Research Square

Preprints are preliminary reports that have not undergone peer review.
They should not be considered conclusive, used to inform clinical practice,
or referenced by the media as validated information.

Structural Engineering and Linear–Nonlinear Optical Properties of Indium Tin Oxide-Modified Poly(vinyl alcohol)/Chitosan Nanocomposite Films

Martin Osemba

osembamartin@gmail.com

Mount Kenya University https://orcid.org/0009-0007-2045-4746

Research Article

Keywords: ITO, Polymer, Optical properties, Flexible optoelectronic application

Posted Date: November 6th, 2026

DOI: https://doi.org/10.21203/rs.3.rs-11629638/v1

License: This work is licensed under a Creative Commons Attribution 4.0 International License.
Read Full License

Additional Declarations: The authors declare no competing interests.

Structural Engineering and Linear–Nonlinear Optical Properties of Indium Tin Oxide-Modified Poly(vinyl alcohol)/Chitosan Nanocomposite Films

Martin Osemba[1]*, Georges Martin[2], Adrián Chávez Huerta[3], Samuel Karenga[1], Godffrey Keru[4]

[1] Department of Natural Sciences, Mount Kenya University, P.O. Box 342-01000, Thika, Kenya
[2] Department of Mathematics, Statistics and Physical Sciences, School of Science and Informatics, Taita Taveta University, P.O. Box 635-80300, Voi, Kenya
[3] Research and Development Division, Fundación Instituto Zuliano de Investigaciones Tecnológicas (INZIT), Km 15 Carretera Vía La Cañada de Urdaneta, Sector Palmarejo Viejo, La Cañada de Urdaneta, Zulia 4033, Venezuela
[4] Department of Chemistry, Whitworth University, 300 W. Hawthorne Road, Spokane, WA 99251, USA
**** Corresponding author: E-mail: mouma@associates.mku.ac.ke***
Martin Osemba: https://orcid.org/0009-0007-2045-4746

ABSTRACT

Polyvinyl alcohol/chitosan (PVA/CS)–based nanocomposite films incorporating indium tin oxide (ITO) nanoparticles were successfully synthesized via a solution-casting technique to investigate their structural, linear, and nonlinear optical properties. ITO nanoparticles were introduced at concentrations of 2–5 wt% to tailor the optoelectronic performance of the polymer matrix. X-ray diffraction analysis revealed a progressive enhancement in crystallinity with increasing ITO content, evidenced by an increase in crystallite size from 25.7 to 32.8 nm and a concomitant reduction in dislocation density and microstrain, indicating improved structural ordering. FTIR and Raman spectroscopy confirmed strong interfacial interactions between ITO nanoparticles and the PVA/CS matrix, including characteristic Sn–O vibrations and shifted ITO phonon modes, validating successful nanoparticle incorporation. SEM and EDX analyses demonstrated uniform nanoparticle dispersion at low loadings, with the onset of agglomeration observed at 5 wt% ITO. UV–Vis–NIR spectroscopy showed a systematic reduction in optical transmittance and a red shift in the absorption edge with increasing ITO content. The optical band gap decreased from 4.49 to 4.13 eV, attributed to the formation of localized states and enhanced electronic interactions within the nanocomposite. Optical constants, dielectric parameters, and dispersion energies derived from the Wemple–DiDomenico and Sellmeier models exhibited pronounced enhancement with ITO loading, reflecting increased polarizability and charge carrier density. Photoluminescence measurements revealed concentration-dependent quenching behavior and defect-related emissions, indicating modified recombination dynamics. Furthermore, significant improvements in third-order nonlinear optical susceptibility ($\chi^{(3)}$) and nonlinear refractive index (n_2) were observed, driven by reduced band gap energy and increased electronic polarization. These results demonstrate that low-level ITO incorporation effectively tailors the structural and optoelectronic properties of PVA/CS nanocomposites, highlighting their strong potential for advanced applications in flexible optoelectronics, photonic devices, nonlinear optics, and sensing technologies.

***Keywords**: ITO, Polymer, Optical properties, Flexible optoelectronic application*

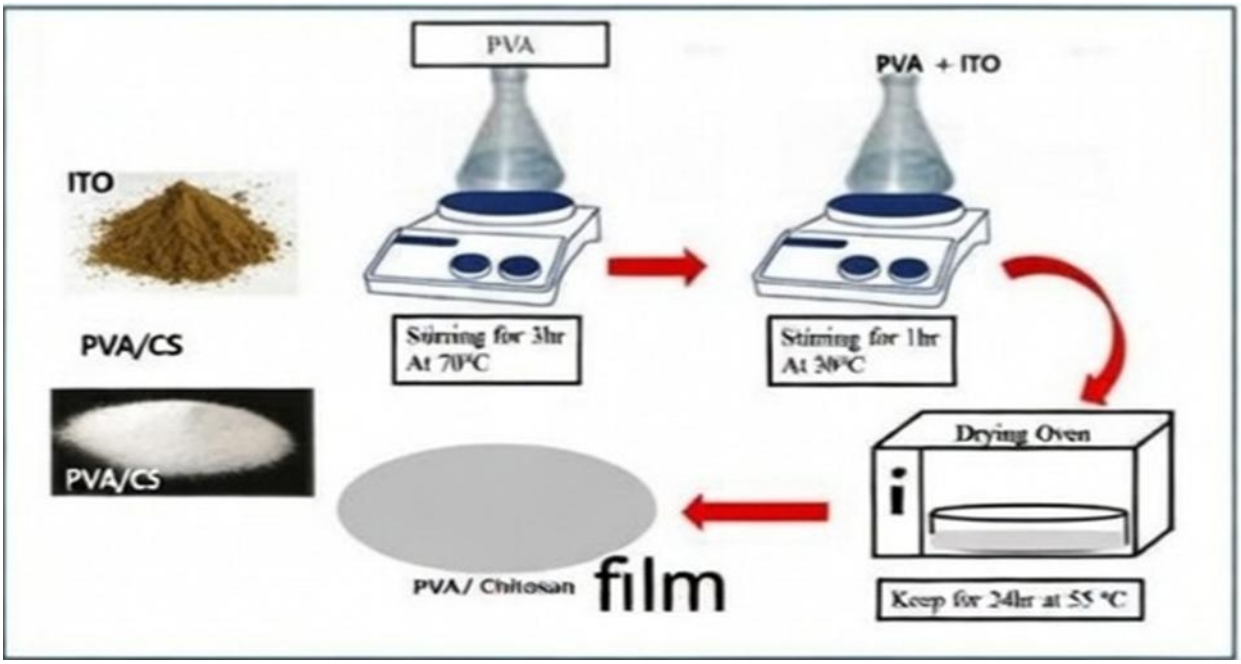
INTRODUCTION

Polymers play a vital role in enhancing optical communication technologies because of their adaptability, affordability, and performance advantages in various photonic applications. In the last ten years, the use of dye-doped polymers has notably risen because of their many benefits, especially in linear and nonlinear photonic devices. Lately, researchers have paid more attention to assessing the optical and electrical characteristics of polymers.[1] The improved polarization, reflection, anti-reflection, and interference characteristics are essential for various technologies, including optical devices. Among numerous essential and commonly used polymers, polyvinyl alcohol (PVA) and chitosan (CS) are notable for their low flammability and exceptional chemical resistance. PVA is primarily used as a sizing and finishing agent in the textile sector. PVA, a man-made linear polymer, exhibits remarkable water solubility, great optical clarity, and outstanding film-forming properties.[2] Its natural biocompatibility, biodegradability, and non-toxicity enhance its usefulness even more.[3] The combination of properties such as processability from aqueous solutions, optical clarity, non-corrosiveness, strong film formation, biocompatibility, and biodegradability facilitates various applications. Specifically, PVA and CS are integrated into water-soluble textiles to create biodegradable products like protective apparel, wipes, sponges, sheets, laundry bags for hospitals, covers, and various personal hygiene items. The optical and electrical properties of polymers can be modified by incorporating dopants such as nanoparticles, organic dyes, quantum dots, and other compatible materials with the primary compound. As a result, polymer-nanoparticle (PNP) composites have attracted considerable research attention as a flexible medium for customizing material characteristics to satisfy particular application needs. These composite systems show improved multifunctional attributes such as thermal, mechanical, optical, and electrical properties in comparison to pure polymers. Additionally, the integration of nanoparticles can enhance the amorphous characteristics of the produced PNP, aiding in these enhancements in performance.[4] The effectiveness of nanocomposite materials in optoelectronic applications can be evaluated by an in-depth study of optical properties such as optical energy gap, optical constants, and dielectric constants, which can be obtained from the spectroscopic properties of PVA/CS nanocomposite films. These parameters are essential for various applications.[5] Tin oxides can serve as dopants/fillers to alter the structural and physical characteristics of PVA/CS polymer blend.[6] Studies have shown that adding tin oxides to PVA/CS matrices results in considerable changes in its characteristics, improving its appropriateness for numerous applications, such as optoelectronics, sensors, and functional coatings. Among tin oxides, ITO has garnered significant interest for photonic uses because of its p-type conductivity and elevated theoretical specific capacity. Unlike TO_2, ITO has unique

physicochemical characteristics and uses. Significantly, ITO is economically advantageous, widely available in nature, and has excellent optical clarity paired with low electrical resistance. These features make ITO an appealing option for future transparent flexible electronic devices. Moreover, ITO is highly suitable for application in electrochromic devices, solar cells, and transparent conductive oxides (TCO). Its increased sensitivity to low gas levels also renders it a valuable material for gas sensing applications. As far as we know, there have been no existing studies that detailed the targeted alteration of structural and linear/nonlinear optical characteristics in PVA/CS matrices by utilizing ITO nanoparticles, which is still inadequately explored. This research gap is important, as ITO nanoparticles provide unique benefits compared to the frequently examined tin dioxide (TO_2), particularly their intrinsic p-type conductivity, an essential feature for new flexible optoelectronic uses such as transparent transistors, hole-transport layers in solar cells, and p-type components in complementary circuits. [25–30, 32–35, 38–40] [19–24]

METHODOLOGY

Integration of Indium tin oxide nanoparticles (ITO NPs) into PVA/CS was done to ensure uniform distribution, consistent film integrity. This process involves reducing nanoparticle clustering PVA/CS- ITO nanocomposite films, ITO nanoparticles were added to the PVA/CS blend at concentrations of 0, 2, 3, 4, and 5 wt% based on 10 grams PVA/CS in terms of weight. To enhance dispersion and reduction of nanoparticle clumping, each mixture was sonicated and then stirred at 30 °C and 900 rpm for 1 hour before casting. The resultant homogeneous solutions were poured into Petri dishes and dried in a convection oven at 55 °C for 24 hours. The schematic diagram below shows the integration of ITO nanofillers to the PVA/CS polymeric matrix.



Scheme 1: The fabrication process of PVA/CS–ITO nanocomposite films.

The percentage weight (wt %) of ITO nanoparticles within the PVA/CS matrix was calculated using the formula below:

$$wITO\% = \frac{wITO}{w_p + wITO} \times 100 \quad \text{.....Eq.1}$$

where ITO signifies the mass of the ITO nanoparticles, and P indicates the mass of the PVA /CS polymeric mixture. This method guarantees an even distribution of ITO nanoparticles throughout the PVA/CS matrix, enabling the examination of their effects on the composite's characteristics.

Characterization of materials

The crystal structures of all materials were examined utilizing the XRD technique (XRD, Bruker D8 Advance with a monochromatic Cu-Kα radiation source λ = 1.54056 Å) functioning at 40 kV and 60 mA within the 2θ = 20–70° range. To analyze the functional groups, FTIR spectra were obtained utilizing a Bruker VERTEX 80 combined. Platinum Diamond ATR features a diamond disc serving as an internal reflector within the range of 4000–400 cm^{-1}, achieving a resolution of 4 cm^{-1}. The Raman spectrum of the PVA/ ITO films was analyzed using a Raman spectrometer (Jasco NRS-2100) at ambient temperature within the spectral range of 80 to 3200 cm^{-1}. Morphology investigation and elemental quantification were performed using a SEM model Quanta FEG250 and an EDS, respectively. The optical characteristics of samples were examined through UV–Vis spectroscopy with a (JASCO 670 UV–vis-NIR)

spectrophotometer over a wavelength range of 200–2500 nm. The emission spectra for the identical sample were recorded using a JASCO FP-8500 spectrofluorometer, with the excitation wavelength established at 330 nm.

RESULTS AND DISCUSSIONS

Structural properties of PVA/ Chitosan/ITO films

Figure 1 displays the XRD for pure PVA/CS film, ITO powder, and PVA/CS infused with varying concentrations of ITO (2, 3, 4, and 5%). The data suggest that pure PVA exhibits a wide peak centered at 2θ = 19.64º, reflecting the semi-crystalline characteristics of the polymer film. The strong hydrogen bonding within each PVA monomer unit and the intermolecular hydrogen bonding among its different monomer units could be responsible for this. The ITO sample displays a pure tetragonal structure with orientations at 18.3, 29.87, 33.3, 37.1, 47.8, 50.7, 57.4, and 62.48° that correspond to the pattern: COD 9,012,140 with orientations in (001), (011), (110), (002), (020), (112), (121), and (013) planes, respectively,37. The PVA peak (at 2θ = 19.64º) decreases as the ITO content rises from 2 to 5%. Furthermore, the strength of the ITO peaks grows with higher ITO concentrations in the films. [36, 37, 41–44]

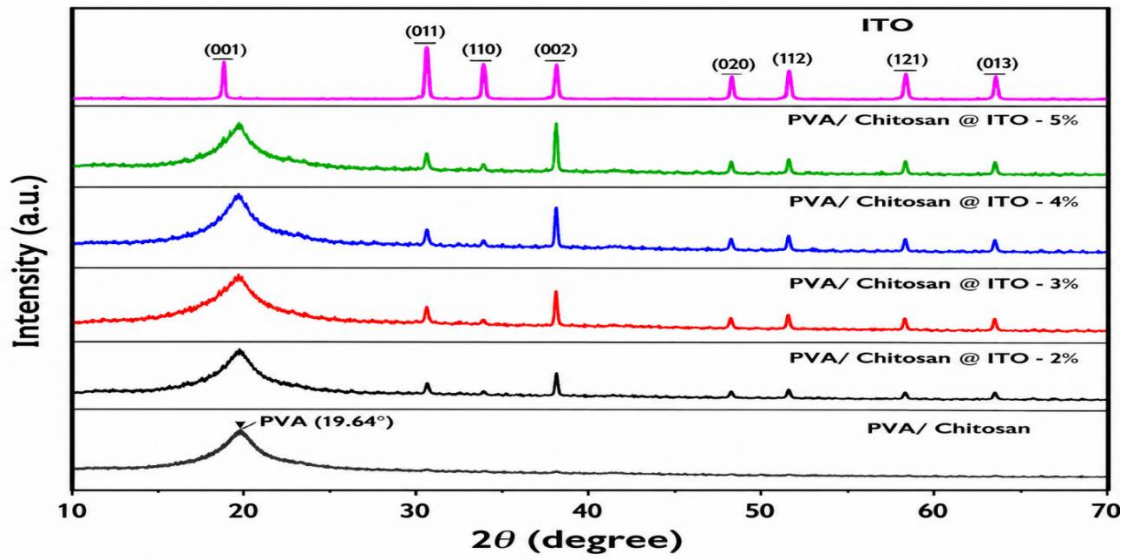


Fig. 1. XRD spectra of PVA/CS films with different levels of ito nanoparticles

Scherrer's equation shown below was used to determine the average crystallite size, D as follows:

$$D = \frac{K\lambda}{\beta cos\theta} \quad \text{.....Eq.2}$$

where, λ represents the Cu-Kα X-ray wavelength (0.15406 nm), θ denotes the Bragg's angle, β signifies the Full Width at Half Maximum (FWHM) in radians, and K = 0.94 is the constant from Scherrer. The diffraction peak's FWHM for the (011) plane clearly indicates the nanosized characteristics of the nanocomposite film. The subsequent equations are utilized to determine the additional microstructural parameters for PVA/CS/ITO nanocomposite films. The dislocation density, δ, defined as the length of dislocation lines per unit volume, is represented by the following equation shown below:

$$\delta = \frac{1}{D^2} \quad \text{.....Eq.3}$$

The following relation is used to compute the micro strain, ϵ_s

$$\varepsilon_s = \frac{\beta \cos\theta}{4} \quad \text{.....Eq.4}$$

Nc, the number of crystallites per unit surface area, is calculated using the following relation:

$$N_c = \frac{d}{D^3} \quad \text{.....Eq.5}$$

In this context, d (≈ 200 ± 5 μm) represents the thickness of the specimen. Table 1 below summarizes the calculated values of crystallite size (D), dislocation density (δ), microstrain (εs), and crystallite number (Nc) at different ITO concentrations. As the ITO concentration increases, the crystallite size increases from 25.71 to 32.83 nm, while the δ, εs, and Nc values decrease, indicating improved crystalline quality. The increase in ITO nanoparticle concentration reduces point-defect density and promotes crystallite growth. Additionally, the Raman mode observed at ~208 cm^{-1} shows an upward shift compared to bulk ITO, confirming the successful incorporation of ITO-NPs into the polymer matrix. These results indicate the formation of high-quality PVA/Chitosan/ITO nanocomposite films.

Table 1. Structural parameters for PVA/ Chitosan/ITO film.

Films	**D (nm)**	**δ (lines·m^{-2}) 10^{15}**	**xε (×10^{-3})**	***Nc (×10^{18} m^{-2})***
PVA/CS − 2% ITO	25.71	1.52	1.406323	5.89

PVA/CS − 3% ITO	28.37	1.23	1.273341	4.36
PVA/CS − 4% ITO	30.21	1.08	1.199825	3.65
PVA/CS − 5% ITO	32.83	0.91	1.101017	2.82

The FTIR spectra of PVA/CS and PVA/CS/ITO nanocomposite films in the wavenumber range of 400–3500 cm^{-1} are shown in Fig. 2(a). To clearly distinguish the characteristic vibrational bands and to highlight the ITO-related peaks, the spectra are presented in two regions: 400–3500 cm^{-1} in Fig. 2(a) and 400–1000 cm^{-1} in Fig. 2(b). In Fig. 2(a), the characteristic peaks of the PVA/CS blend appear at 3269 cm^{-1} corresponding to O–H stretching vibrations, 2906 cm^{-1} due to asymmetric stretching of CH_2 groups, 1711 cm^{-1} attributed to C=O stretching of residual acetate groups, 1417 cm^{-1} assigned to CH_2 bending, and 1325 cm^{-1} related to C–H bending. The band at 1141 cm^{-1} is associated with O–H bending, while the peak at 1087 cm^{-1} corresponds to C–O stretching vibrations. Additional bands at 916 cm^{-1} and 843 cm^{-1} are assigned to CH_2 rocking and C–C stretching, respectively. In Fig. 2(b), the presence of a sharp absorption band around 598 cm^{-1} is attributed to the Sn–O stretching vibration, confirming the incorporation of ITO nanoparticles into the polymer matrix. [26–31, 45]

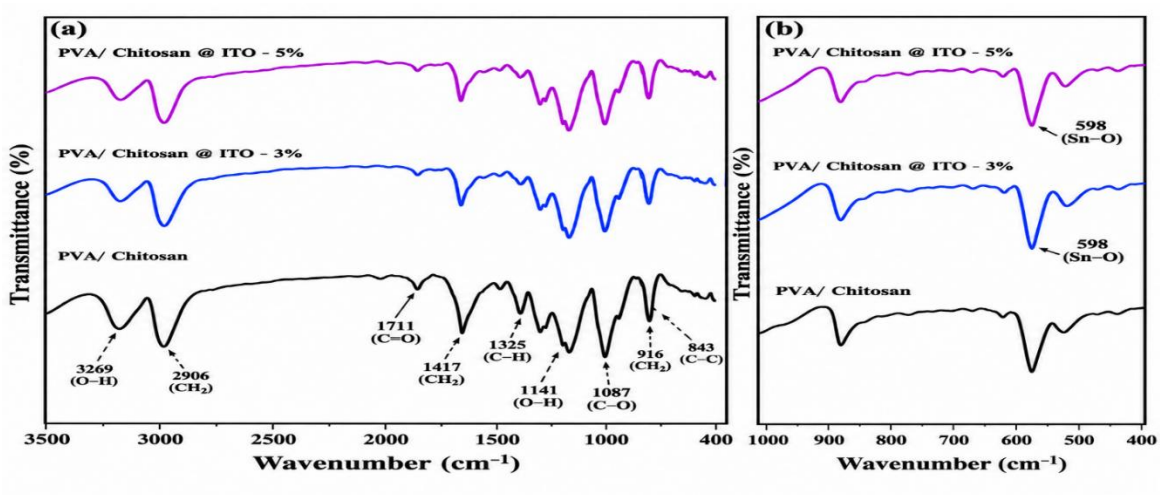


Fig. 2. FTIR spectra of PVA/CS and PVA/CS @ITO (3 and 5 wt%)

Raman spectroscopy offers a reliable approach to identify nanoparticles and investigate their interactions with polymers through the analysis of changes in peak positions and intensities. The spectra of ITO at 5% doped PVA/CS and pure PVA/CS films shown in figure 3 below reveal distinct vibrational modes, including a significant band around 2900 cm^{-1} linked to the C–H stretching vibrations of $–CH_2$ groups in the PVA/CS matrix. Other vibrational features are also present, such as 1324 cm^{-1} (CH_2 wagging/C–H bending), 904 cm^{-1} (C–C stretching), 637 cm^{-1} (C–O–C bending), 465 cm^{-1} (C–C bending), and 281 cm^{-1} (skeletal bending), found in both the ITO -doped PVA/CS and the undoped sample. The addition of ITO causes this mode to change in both position and intensity, indicating that the ITO nanoparticles are interacting with the PVA/CS matrix and altering its local chemical surroundings. Significantly, the appearance of ITO specific Eg and A_1g modes at 105 and 206 cm^{-1} respectively, shifted upward compared to bulk ITO, confirms the successful integration. The films' surface morphology is examined using SEM to assess the impact of surface modification.

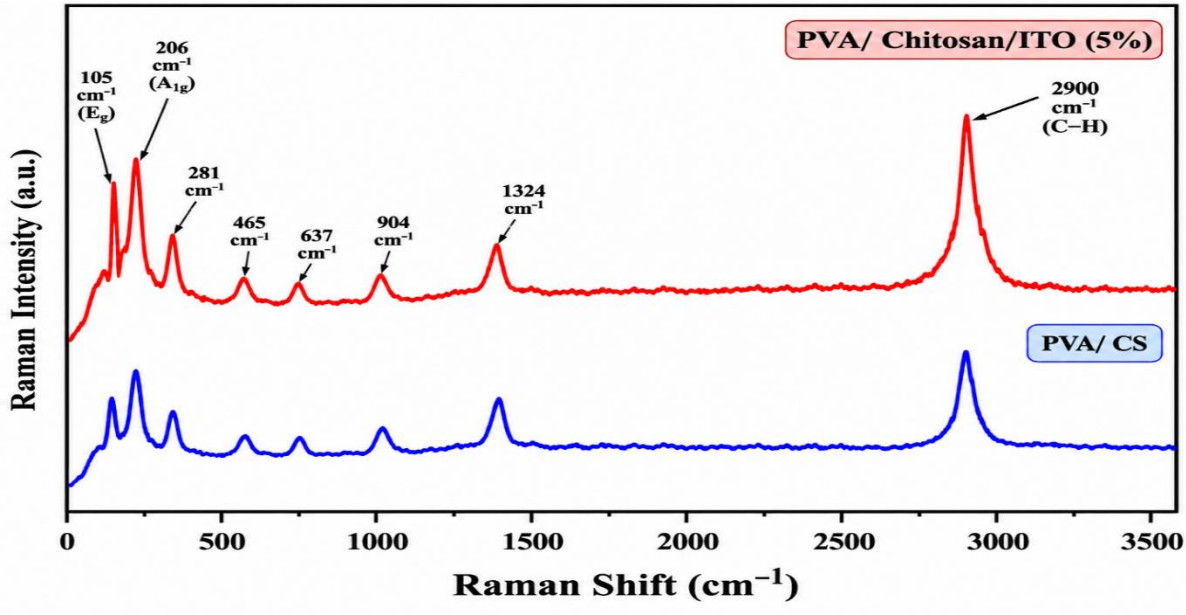


Fig. 3. Raman spectra for pure PVA/CS and PVA/ Chitosan/ITO (5%) film.

Figures 4a shows SEM surface morphologies of PVA/CS/ITO at 5 wt% films. The pure PVA/CS film exhibits a smooth and homogeneous surface, indicating good polymer compatibility. At 2 wt% ITO loading, nanoparticles are uniformly dispersed within the matrix, causing negligible morphological changes. In contrast, the 5 wt% ITO film shows pronounced nanoparticle agglomeration and clustered regions, accompanied by increased apparent particle size and reduced interparticle spacing. This behavior is attributed to enhanced filler–filler interactions at higher ITO

concentrations, consistent with earlier reports. The increased surface roughness and high surface area of ITO nanoparticles contribute to the functional enhancement of the nanocomposite, supporting its suitability for gas-sensing applications. Figure 4a presents the cross-sectional SEM image of the PVA/CS/ITO–5 wt% film, revealing a uniform thickness. Thickness measurements obtained at five different locations using ImageJ yielded an average value of 200 µm, ensuring statistical reliability for optical property calculations. The corresponding EDX spectrum (Fig. 4b) confirms the presence of C, O, In, and Sn, verifying the successful incorporation of ITO into the PVA/CS matrix.

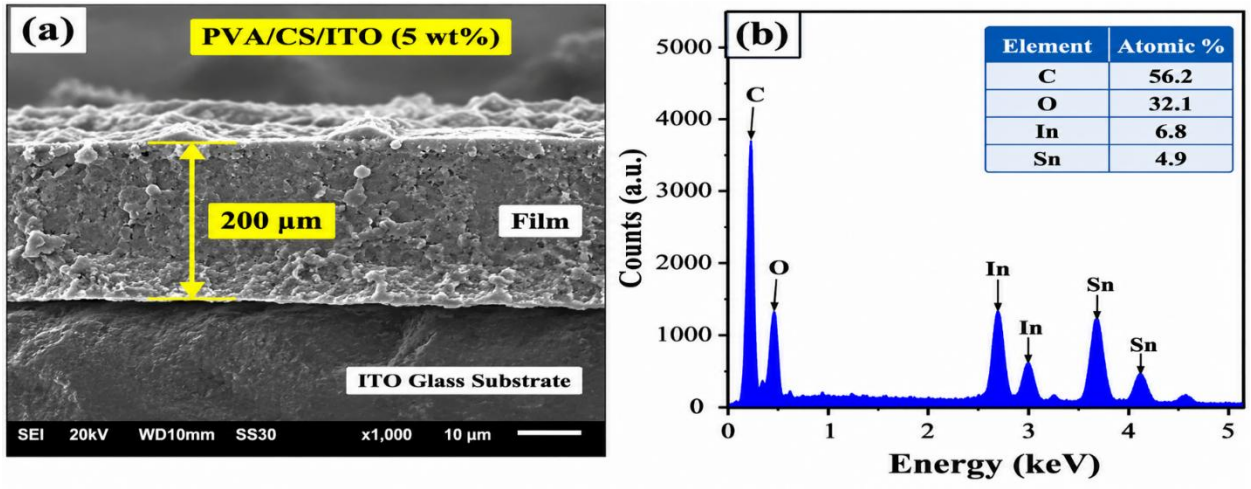


Fig. 4. (a) Cross-sectional SEM image of the PVA/CS/ITO (5 wt%) film and (b) the corresponding EDX spectrum.

Optical characterizations of PVA/Chitosan/ITO nanocomposite films

Optical band gap

The transmittance, and reflectance, spectra of pure PVA/CS and PVA/Chitosan/ITO nanocomposite films were investigated over the wavelength range of 200–2500 nm. As shown in Fig. 5(a), the transmittance of the films decreases noticeably with increasing ITO concentration, accompanied by a shift in the absorption edge (cut-off wavelength). This reduction in transmittance can be attributed to increased light scattering arising from surface roughness and grain growth induced by the incorporation of ITO nanoparticles Ouma, O., Martin. The pure PVA/CS film exhibits high optical transparency, with a transmittance of approximately 91.14% at 400 nm. In contrast, the transmittance progressively decreases to 84.77%, 74.2%, 69.8%, and 56.55% for films containing 2, 3, 4, and 5 wt% ITO, respectively. The reflectance spectra presented in Fig. 5(b) show a sharp decrease in reflectance within the 200–250 nm region, which is associated with the optical band gap of the material and reflects the semicrystalline nature of the PVA/CS matrix. With increasing ITO content, the reflectance gradually increases due to enhanced photon

scattering and increased refractive index mismatch. Furthermore, visual observation reveals a gradual colour change from transparent for pure PVA/CS to semi-transparent for the ITO-loaded films, indicating enhanced light absorption over a broad spectral range in the nanocomposite materials. [46–52]

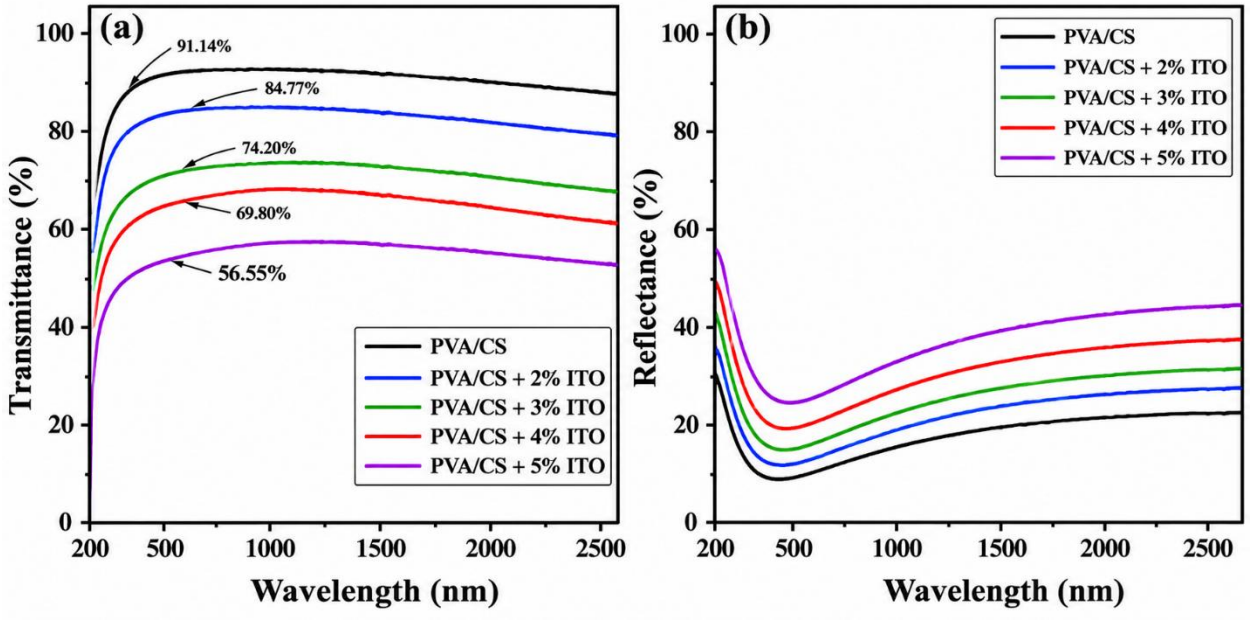


Fig. 5. UV–Vis–NIR Transmittance (a) and Reflectance (b) Spectra of PVA/Chitosan and PVA/Chitosan/ITO Nanocomposite Films

These observations further confirm the significant influence of ITO incorporation on the optical properties of the PVA/CS matrix. The T (λ) optical transmittance, was used to evaluate the absorption coefficient (α) according to the relation:

$$\alpha = \frac{1}{d}\ln\left(\frac{1}{T}\right) \quad \text{.....Eq.6}$$

where is the thickness of the film. The variation of the absorption coefficient as a function of wavelength for PVA/Chitosan/ITO nanocomposite films with different ITO contents is presented in Fig. 6(a). The absorption behavior near the fundamental absorption edge was employed to determine the optical energy band gap of the films. The dependence of the absorption coefficient on the photon energy is described by the Tauc relation:

$$\alpha h\nu = A\left(h\nu - E_g^{Opt}\right)^r \quad \text{..... Eq.7}$$

where A is a constant, E_g^{Opt} is the optical band gap, and r is an exponent that depends on the nature of the electronic transition.

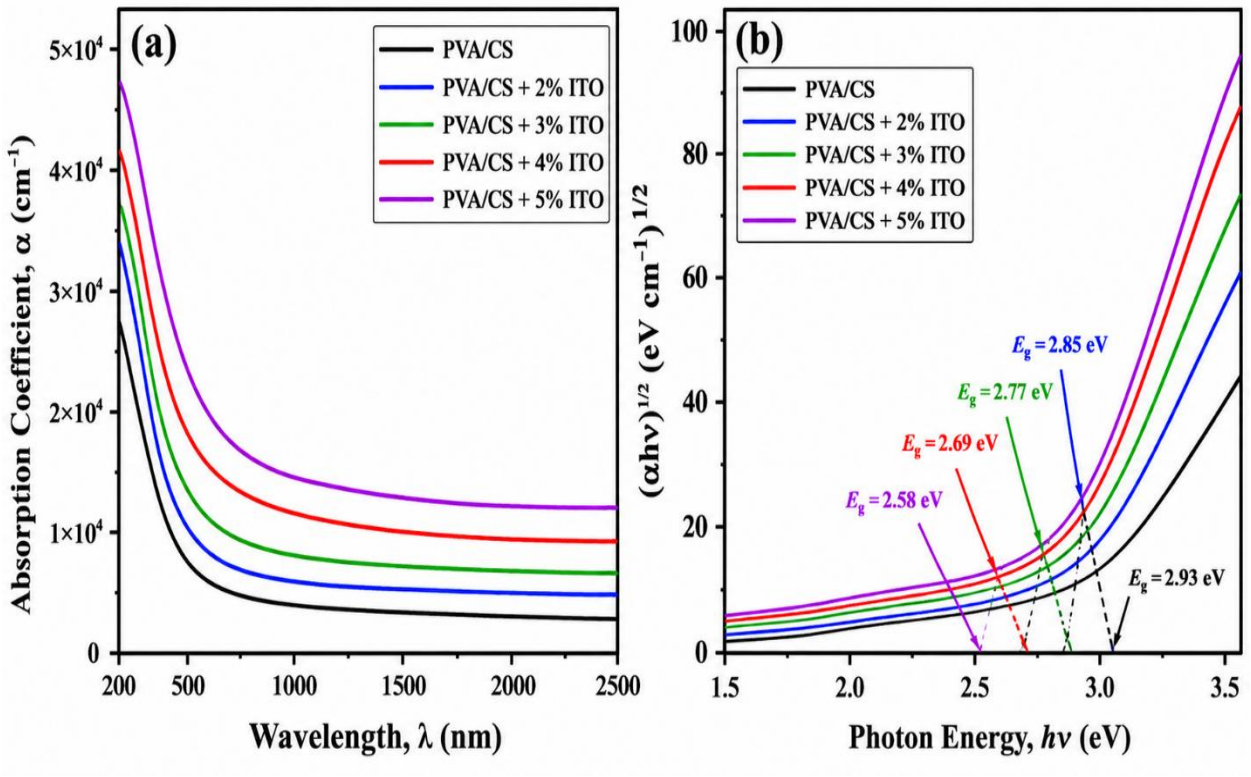


Fig. 6. (a) Absorption coefficient (α) as a function of wavelength (λ) and (b) Tauc plots of $(\alpha h\nu)^{1/2}$versus photon energy (hν) for PVA/Chitosan/ITO nanocomposite films with different ITO contents.

Table 2. Optical and dielectric parameters derived from UV–Vis spectroscopy and the Wemple–DiDomenico model of PVA/CS/ ITO films

$E_o$pt (eV)	3.48	3.36	3.2	3.21	3.07
E_o (eV)	5.17	6.03	5.68	5.57	5.35

E_d (eV)	8.17	10.12	11.52	12.52	14.71
ϵ_∞ **WD**	1.36	2.56	2.19	3.31	3.65
n_o	1.46	1.36	1.17	1.67	1.77
(m^{-2}) × 10^{13}	0.26	0.54	3.6	5.70	5.535
λ_o (nm)	280	247	45.61	49.67	32.52
ε_l	1.24	2.55	2.96	2.89	3.82
$\frac{N}{m^*}$ **x 10^{49}**	6.588	12.187	13.36	14.203	17.13
n_2 **x 10^{-12} ($h\upsilon \rightarrow 0$)**	0.768	1.16	2.40	2.88	5.78
$\chi^{(3)}$ **x 10^{-13} ($h\upsilon \rightarrow 0$)**	0.313	0.443	0.817	1.14	2.49

Table 3. Comparison of optical band gap (E_o) of PVA/CS nanocomposites with various nanofillers from literature and current work

c	Nanofiller	Ratio (wt %)	Eg (eV)	Reference
PVA/CS	CuO	0-0.4	5.30–4.50	[14]
PVA/CS	Al_2O_3	1–3	4.93–4.88	[15]
PVA/CS	$CaThO_3$	0–4	5.1–4.60	[16]

PVA/CS	Co^{+}	0.1–10	4.95–4.02	[17]
PVA/CS	Fe_2O_3	1	4.79	[18]
PVA/CS	NiO	1	5.01	[7]
PVA/CS	ITO	2–5	4.49–4.13	Current work

where $E_o$pt denotes the optical energy band gap, r is an exponent that can take values of 1, 2, 3, 1/2, or 3/2 based on the electronic transitions responsible for the optical absorption, A represents a constant, and hυ indicates the energy of the photon. The values of the optical energy gap for each electronic transition are determined by extending the linear segments of the curves to (α hυ) /2 = 0 (refer to Fig. (6b)) and are listed in Table 2 above. It is evident that as the concentration of ITO rises, the values of the optical band gap decrease. The results obtained indicate that the bandgap characteristics of PVA/ Chitosan/ITO nanocomposites can be efficiently adjusted by changing the ITO -to-PVA/CS ratio in the mixture. In addition, the inclusion of ITO promotes the development of a three-dimensional (3D) interconnected structure within the polymer matrix, establishing conductive pathways that improve the semiconducting characteristics of the composite. This change in structure results in a decrease in the optical bandgap from 4.49 to 4.13 eV, as demonstrated by the information provided in Table 2. These results emphasize the capability of ITO as a functional filler for customizing the electronic and optical characteristics of PVA-based materials. The $E_o$pt values presented in Table 3 offer significant insights regarding our study in relation to previous research. This research on PVA/ Chitosan/ITO nanocomposites distinguishes itself from previous studies by incorporating a minimal quantity of ITO nano-fillers (2–5 wt%), leading to a notable reduction in the indirect $E_o$pt to 4.13 eV. This enhancement differs from documented nanocomposites using various fillers (e.g., Al_2O_3, $CaThO_3$, Co^{+}, CuO, Fe_2O_3, NiO, TiO_2). Therefore, this necessitated greater filler amounts (e.g., as much as 10 wt% for Co^{+}) to achieve similar bandgap alteration. The performance of ITO at this reduced level results in values that are comparable to those from established $E_o$pt.

Photoluminescence properties for PVA/ Chitosan/ITO film

The photoluminescence (PL) emission spectra of pure PVA/CS and PVA/ Chitosan/ITO (2, 3, 4, and 5%) are analyzed, as illustrated in Fig. 7. The PL spectra are obtained with an excitation wavelength of 330 nm. The PVA/CS film

exhibited a distinct luminescence peak in the visible spectrum, spanning from 350 to 550 nm. The peak at 379 nm is associated with the electronic transition (π* → n) of the hydroxyl groups present in PVA/CS, while the peak at 405 nm corresponds to (π → π*) electronic transitions of the free hydroxyl (–OH) groups within the PVA matrix.[7] The incorporation of ITO into the PVA/CS matrix led to a notable reduction in the luminescence intensity. The quenching effect is attributed to the establishment of cross-linking interactions between the (–OH) groups of PVA and the oxygen atoms of SnO.[8] The interactions alter the electronic landscape of the PVA/CS matrix, that diminishes the mechanisms responsible for generating light, referred to as radiative recombination.

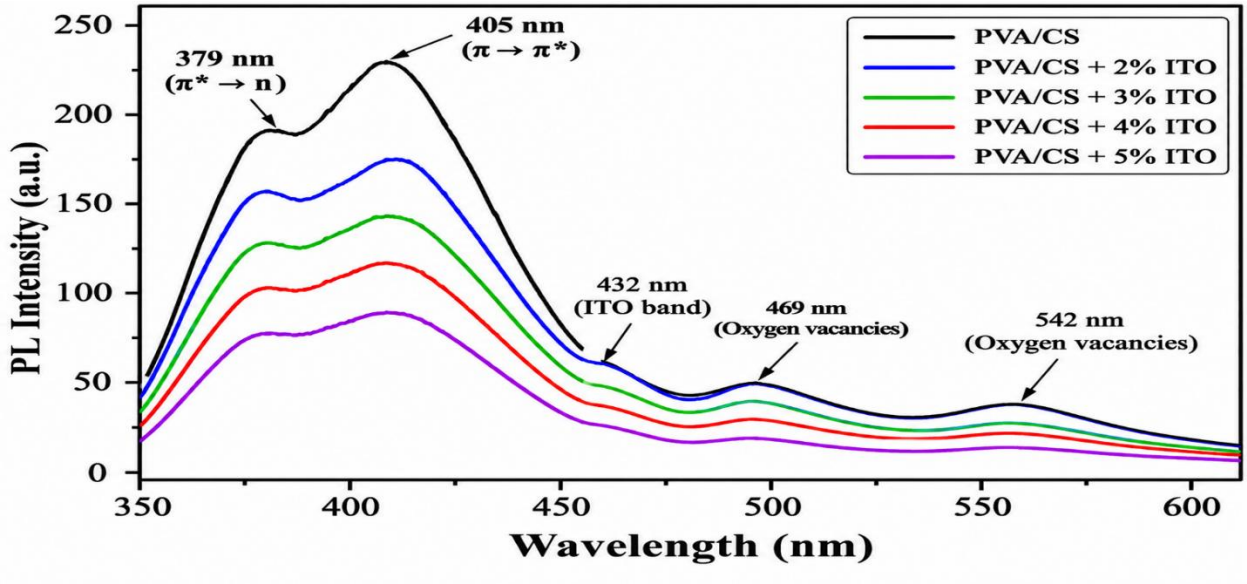


Fig. 7. PL vs. wavelength (nm) for nanocomposite PVA/ITO film.

The degree of quenching is observed to be reliant on concentration, with increased ITO levels leading to more significant quenching effects. In particular, at (4 and 5%) films exhibited three emission peaks located around 432, 469, and 542 nm. The emission band at 432 nm corresponds to the band emission of ITO, in line with its band gap range of 2.7–3.4 eV.[6] The peaks observed at 469 and 542 nm are probably associated with defects like oxygen vacancies. Consequently, the PL spectrum of PVA/ Chitosan/ITO appears to reflect contributions from both PVA/CS and ITO nanoparticles this in line with the previous findings.

Dispersion and optoelectronic characteristics

The absorption coefficient (α) and reflectance R (λ) are utilized to calculate the optical constants, specifically the refractive index n and the extinction coefficient k, through the following equations as reported previously.[9] Figure (8a) illustrates how the extinction coefficient k changes with wavelength for PVA/ Chitosan/ITO films that has different amounts of ITO. The extinction coefficient values for PVA films are less than those for PVA/ Chitosan/ITO films. The deposited nanocomposite films demonstrated favorable optical transparency, evidenced by the low extinction coefficient observed in the visible-NIR wavelength ranges, indicating minimal light loss due to scattering.

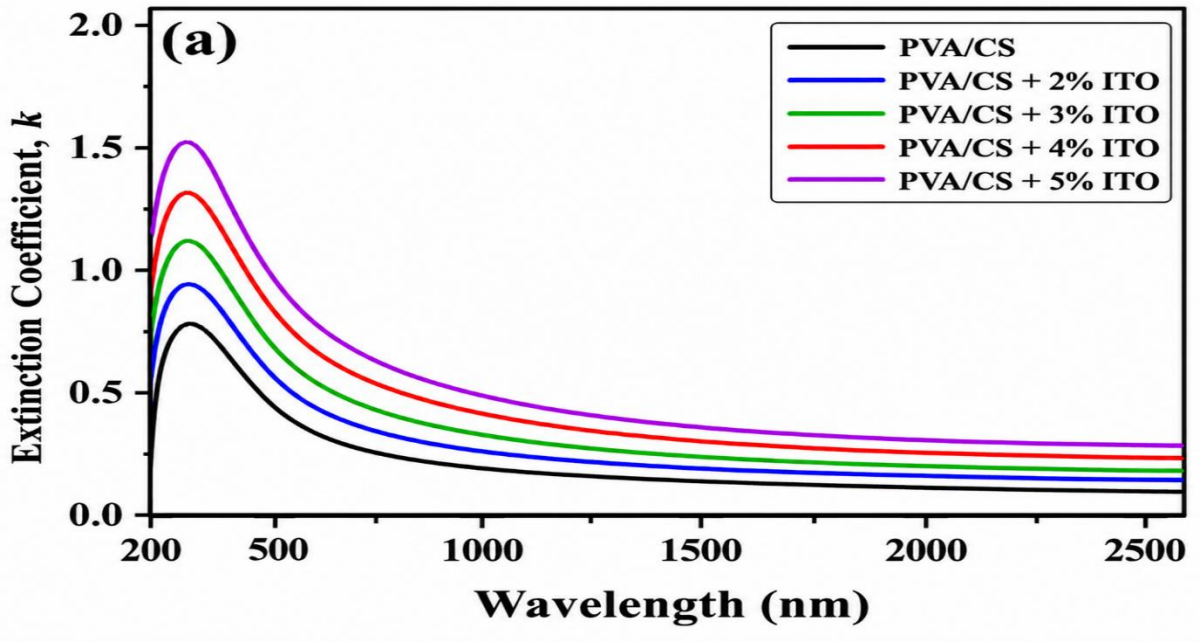


Fig. 8(a). Wavelength-dependent extinction coefficient (k) of PVA/Chitosan and PVA/Chitosan–ITO nanocomposite films at different ITO loadings

The change in the refractive index, n, with wavelength for the samples is illustrated in Fig. (8b). An increase in ITO content is also noted to result in a parallel rise in the refractive index of PVA/ Chitosan/ITO composites. The addition of ITO NPs (5 wt%) to the PVA matrix raises the refractive index from 1.641 (untreated PVA) to 2.27 at λ = 400 nm. This 26% improvement results from two complementary factors: (i) the naturally high polarizability of Sn^{2+} ions and (ii) matrix densification caused by ITO/PVA hydrogen bonding (validated by FT-IR/Raman). Importantly, this performance surpasses that of PVA/SiO_2 nanocomposites (Δn = 18% at 10 wt%) and nears the PVA-CoO-$SiO_2$62 ternary systems (n ≈ 2.7 at 6 wt%), while needing less filler content and a more straightforward binary composition. The elevated refractive index (n > 2.0 throughout visible wavelengths) enables improved optical confinement, making

these films strong contenders for waveguides and high-performance optical filters and nonlinear photonic devices utilizing strong field-matter interaction.

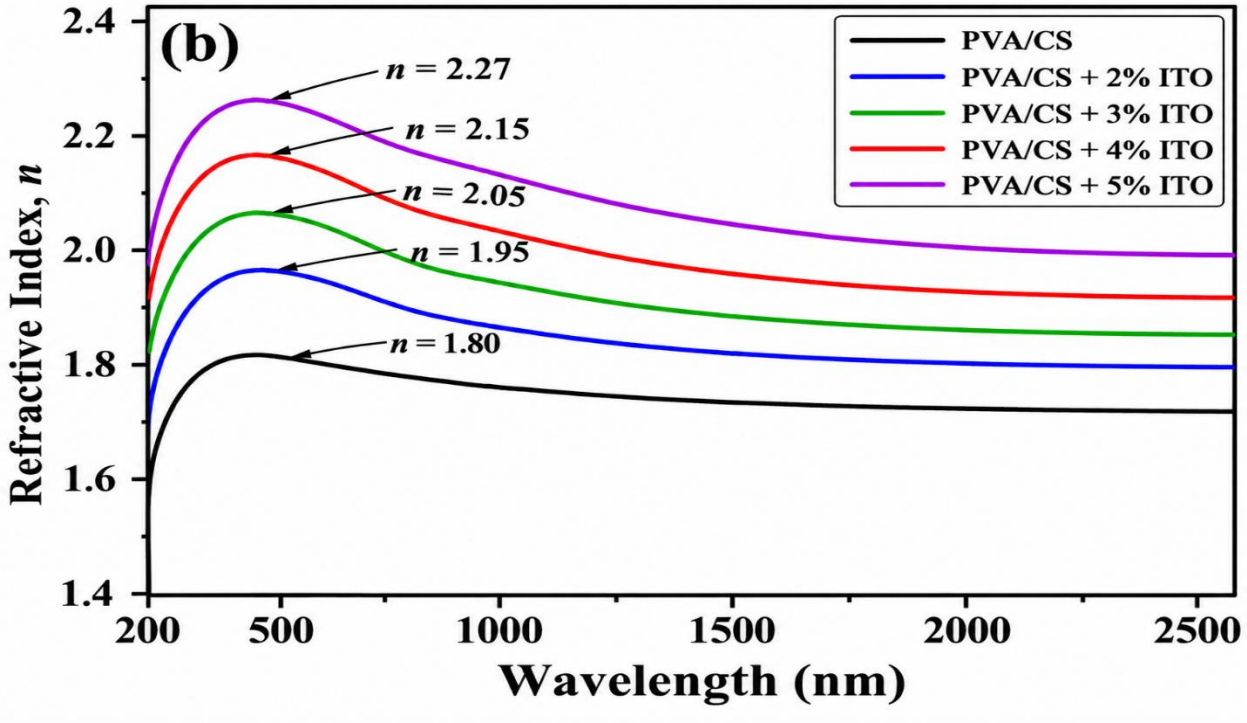


Fig. 8(b). Wavelength-dependent refractive index (n) of PVA/Chitosan and PVA/Chitosan–ITO nanocomposite films at different ITO loadings.

The high-frequency refractive index of an optical substance can be found utilizing an approximate relation based on the single oscillator model introduced by Wemple and DiDomenico.[10] [10, 53–57]

$$k = \frac{\alpha\lambda}{4\pi} \quad \text{..... Eq.8}$$

$$n = \frac{1+R}{1-R} + \sqrt{\frac{4R}{(1-R)^2} - k^2} \quad \text{..... Eq.9}$$

where, Ed is the dispersive energy, which represents the average intensity of inter-band optical transitions, and Eo is the single oscillator energy. As the (n2 − 1) −1 vs. (hv)2 plot for PVA/ Chitosan/ITO films is shown in Fig. (9a) to be

of these trajectories rise from 9.28 to 14.17 eV. The Eo values decreased from 6.28 to 5.53 eV, indicating a lower average energy gap related to the oscillator.

ITO /PVA films (5 wt%) demonstrated enhanced dispersion characteristics and optical efficacy, as indicated by their notably elevated dispersion energy (Ed = 14.17 eV) and single oscillator energy (Eo = 5.53 eV) relative to PVA/CS/CuO (5 wt%) (Ed = 2.54 eV, Eo = 4.24 eV) and PVA/TiO_2 (5 wt%) (Ed = 11.8 eV, Eo = 2.75 eV) and PVA/TiO_2/MWCNT (0.01mg) (Ed= 7.75 eV, Eo = 2.52 eV). This improved Ed demonstrates greater inter-band optical transitions and charge carrier interactions, whereas the increased Eo signifies a more organized electronic structure with fewer defects. Importantly, ITO accomplishes this with merely 5 wt% loading, which is lower than standard filler amounts in rival systems, resulting in significant decreases in optical bandgap (28% reduction), and reduced nanoparticle clustering.[11] This behavior indicates how ITO incorporation affects the electronic configuration and optical characteristics of the PVA/CS matrix, underscoring the capability to customize these composites for targeted optoelectronic applications. By extending hv → ∞, the Wemple-DiDomenico model yields the high-frequency dielectric constant ε:

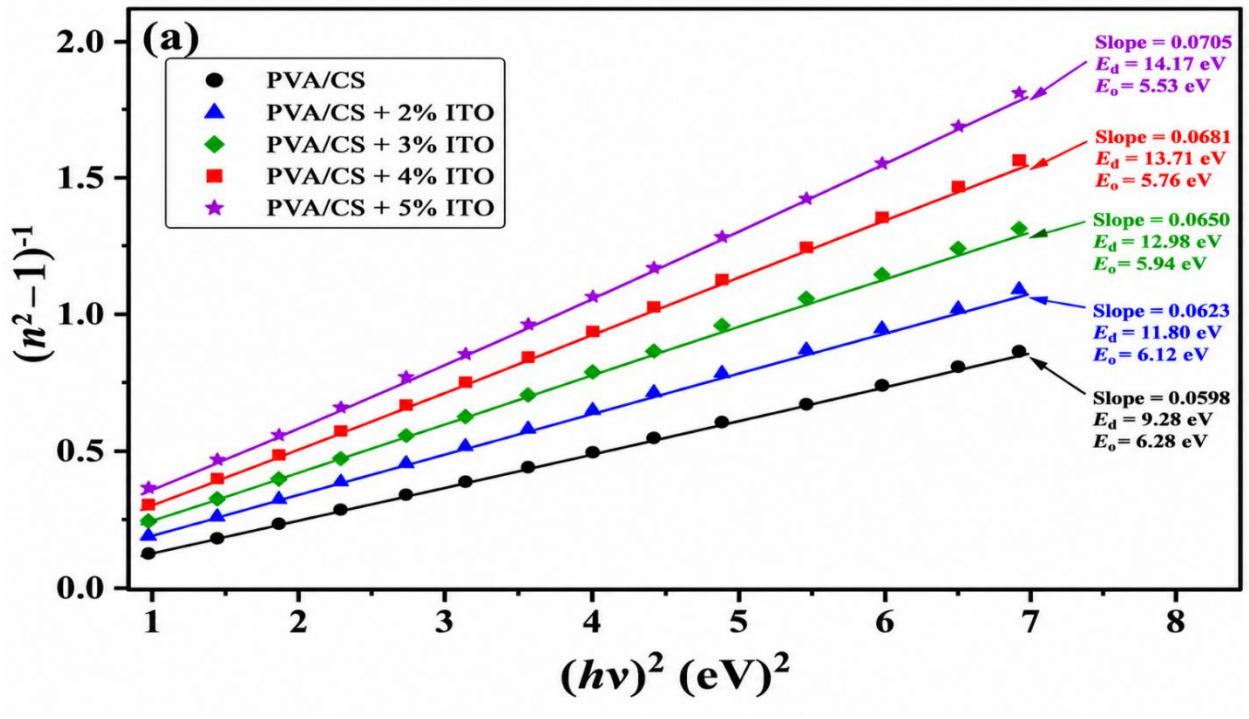


Fig. 9. (a) Plots of $(n^2 - 1)^{-1}$ versus $(hv)^2$ for PVA/CS/ITO films.

In contrast, the formula for calculating the value of static refractive indices () is =. The value of ITO nanoparticles. Such concentration-dependent optical properties make these nanocomposite films highly attractive for photonic applications, including waveguides, and optical filters. The single-term Sellmeier oscillator model may also be used to study the refractive index, where, λo represents the average wavelength of the oscillator and S_o denotes the average wavelength of the oscillator. The graph of (n2 − 1) −1 versus λ−2 for the PVA/ ITO nanocomposite films is illustrated in Fig. (9b). Table (2) presents the values of So and λo, derived from the linear fitting of the plots.

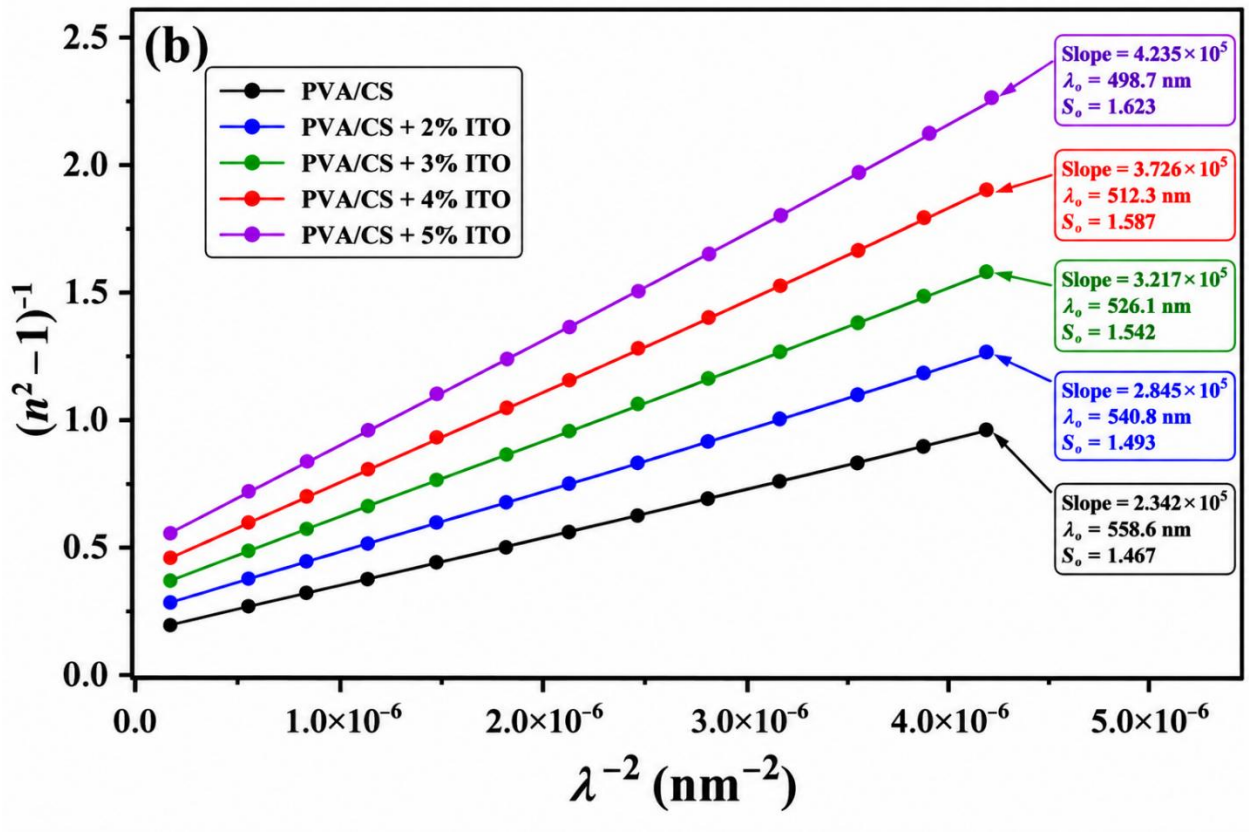


Fig. 9. (b) Plots of (n2−1) −1 vs. λ−2 for PVA/ Chitosan/ITO films

Optical dielectric characteristics of pva/ ITO nanocomposite films

Although a spectrophotometer cannot directly assess dielectric parameters through experimentation, these parameters can be determined using the equations obtained from the n and k data:[12] [58–62]

$\epsilon = \epsilon_1 + j\epsilon_2 \quad \epsilon_1 = n^2 - k^2 \quad \epsilon_2 = 2nk$ …… Eq.10

where, ε_1 and ε_2 denote the real component (optical dielectric constant) and the imaginary component (optical dielectric loss) of the dielectric constant, respectively. Figures 10 shows how ε_1 and ε_2 vary with wavelengths. As illustrated in Fig. 10(a), the ε_1 stays almost unchanged with rising wavelength, signifying a stable optical characteristic within the measured interval.

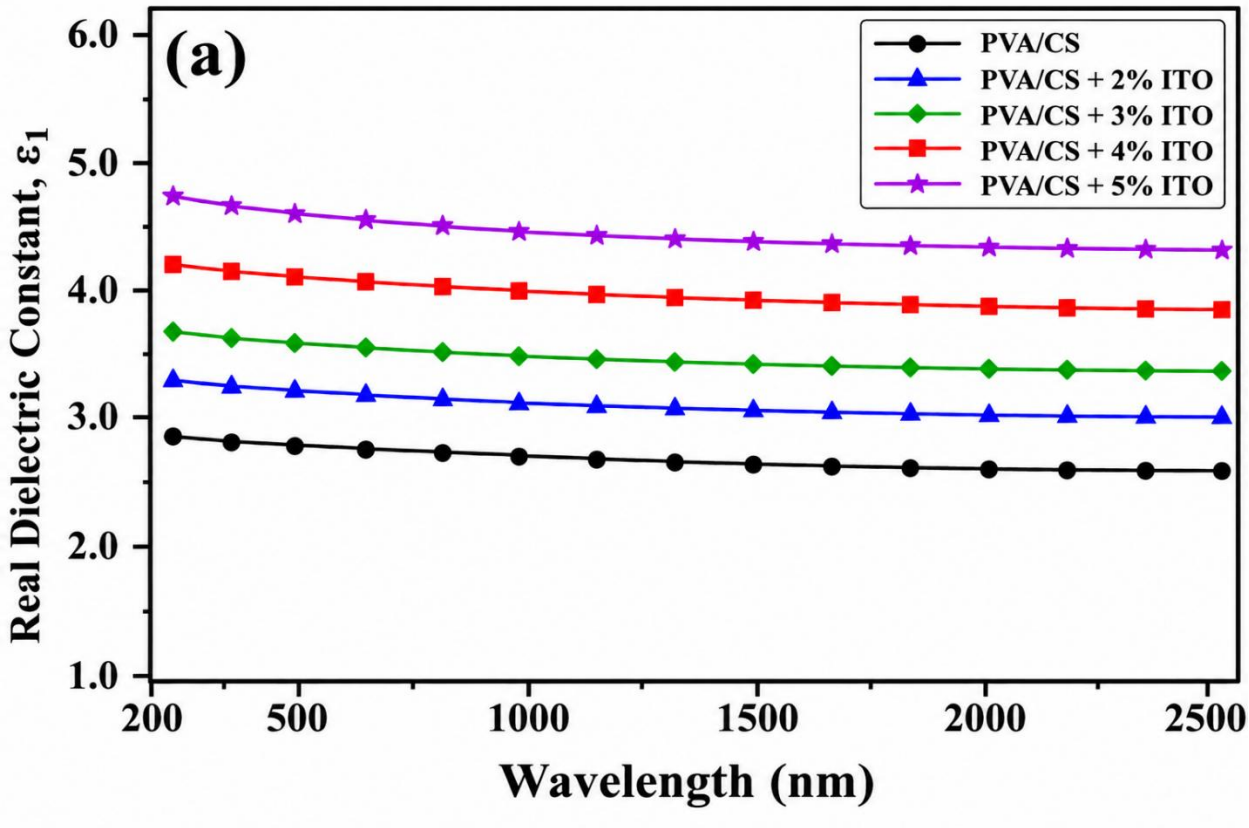


Fig. 10(a). Variation of the real part of the dielectric constant (ε_1) as a function of wavelength for PVA/Chitosan/ITO films.

In comparison to Fig. 10(b) which shows that the ε2 has a linear rise with wavelength across all samples, indicating the material's absorption properties.

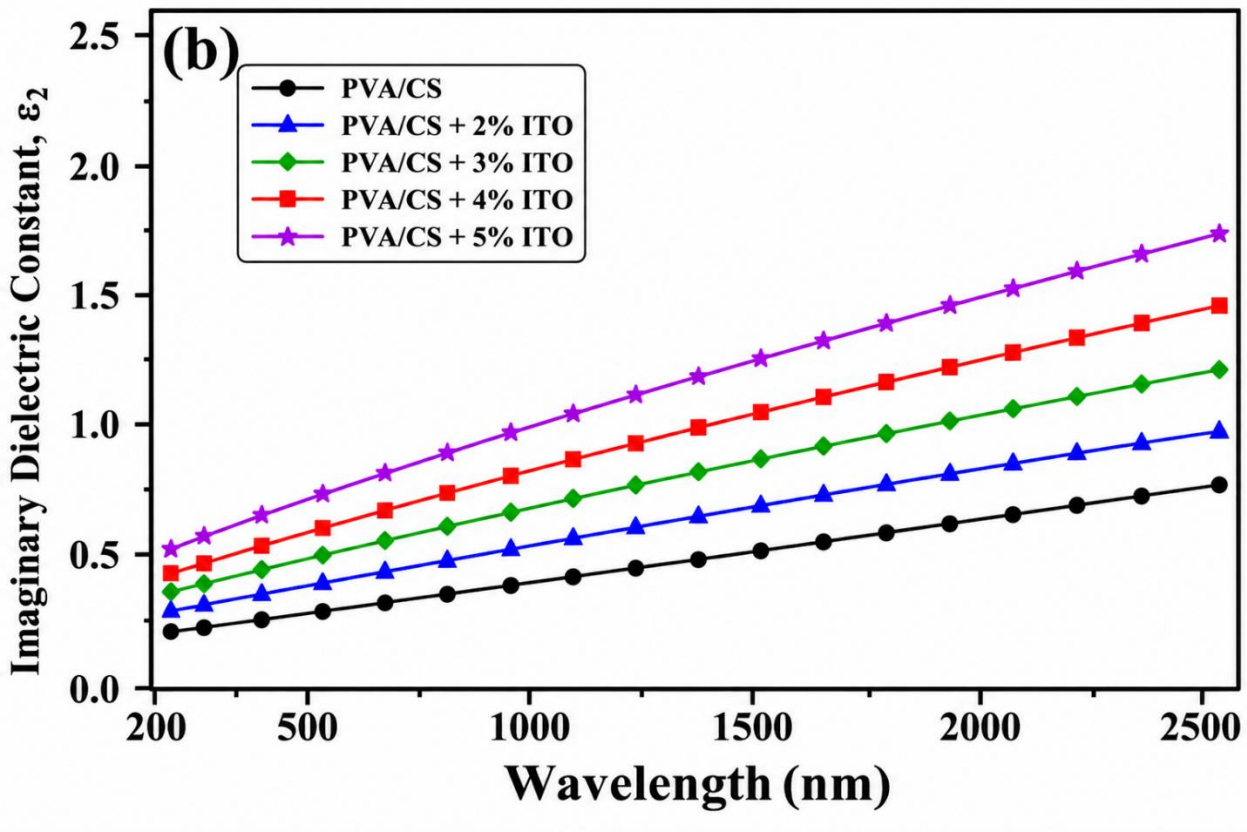


Fig. 10(b). Variation of the imaginary part of the dielectric constant (ε_2) as a function of wavelength for PVA/Chitosan/ITO films

The imaginary component of the dielectric function is strongly linked to the absorption coefficient and is mainly affected by electron transitions from filled to unfilled states. Moreover, as the ITO nanoparticle concentration in the PVA/CS matrix increases, both ε1 and ε2 exhibit a corresponding increase, as illustrated in Fig. (10). This trend corresponds with the noted rise in the n and k values. The improved dielectric characteristics with greater ITO levels can be linked to the heightened polarizability and densification of the nanocomposite films, enhancing their optical and electronic performances. These results emphasize the promise of PVA/CS/ITO nanocomposites for use in optoelectronic devices, including sensors, photodetectors, and energy storage systems, where adjustable dielectric properties are crucial. The capability to manipulate these characteristics via ITO concentration further highlights the adaptability of these materials for cutting-edge technological uses.[12] The relationship between the ε1 and λ2 in the transparent area can be expressed as follows:

$$\epsilon_1 = n^2 - k^2 = \epsilon_L - \frac{e^2}{4\pi^2\epsilon_0 c^2}\left(\frac{N}{m^*}\right)\lambda^2 \quad \text{..... Eq.11}$$

where, εL denotes the lattice dielectric constant, e is the fundamental charge, c represents the speed of light, and N/m signifies the ratio of carrier density to the effective mass. Values of εL and N/m are obtained from the intercept (λ2 = 0) and the slope of the linear fit for PVA/CS/ITO nanocomposite films, as shown in Fig. (11); these values are presented in Table 2. Table 2 shows that εL rises with increased ITO content, suggesting improved dielectric properties from the addition of ITO nanoparticles.

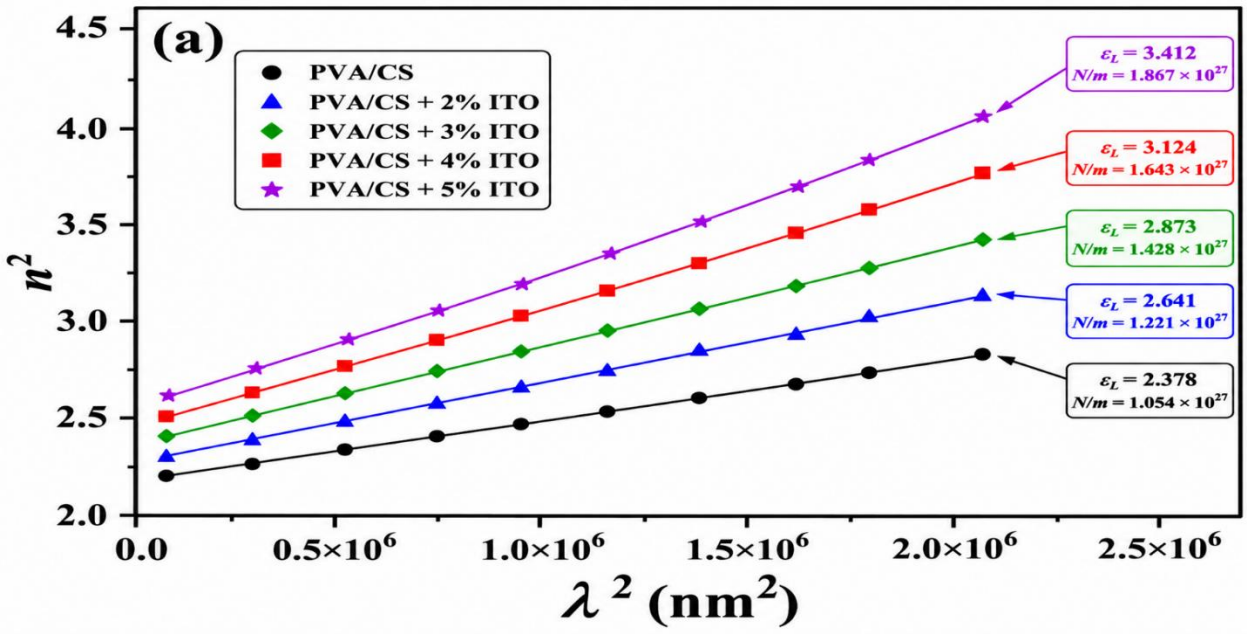


Fig. 11. Plots of n^2 versus λ^2 for PVA/Chitosan/ITO films at different ITO loadings.

Moreover, the values of εL are always greater than those of the dielectric constant (ε∞) at high frequencies. This difference can be ascribed to the rise in free carrier concentration in the nanocomposite films, which enhances the lattice polarization and the general dielectric response. The increase in free carrier concentration with higher ITO content additionally improves the material's electrical and optical characteristics, rendering it appropriate for use in optoelectronic and photonic applications. The capability to adjust εL and N/m* by altering the ITO concentration highlights the promise of PVA/ Chitosan/ITO nanocomposites for cutting-edge technological uses, including sensors, energy storage systems, and optical films. These results emphasize the essential function of ITO nanoparticles in altering the dielectric and electronic characteristics of the PVA matrix, providing a means for creating materials with

customized functionalities. The characteristics of energy loss in a material can be explained through two main functions: the surface energy loss function (SELF) and the volume energy loss function (VELF). The SELF denotes the energy lost by electrons when they interact with the surface of the material, whereas the VELF relates to the energy loss of rapid electrons moving through the interior of the material. Both functions are based on the ε1 and ε2, which are computed utilizing the subsequent relationships. The VELF offers information on the overall electronic characteristics and energy loss processes in the material, whereas the SELF is especially valuable for examining surface interactions and plasmonic phenomena. These functions are essential for examining the optical and electronic properties of materials, particularly in applications related to electron energy loss spectroscopy (EELS) or surface plasmon resonance (SPR). The relationship between VELF and SELF with respect to ε1 and ε2 underscores the significance of dielectric characteristics in influencing energy loss processes. For example, substances with elevated ε2 values generally demonstrate enhanced energy dissipation owing to greater absorption and electronic transitions. Through the analysis of these functions, researchers can acquire important knowledge regarding the material's optical response, electronic configuration, and possible uses in areas such as plasmonic, optoelectronics, and energy harvesting. The total energy loss is indicated by the values of VELF and SELF. Figure 12(a&b) illustrates the VELF and SELF as a function of wavelength for PVA/CS/ ITO nanocomposite films. SELF and VELF display comparable patterns. Furthermore, at that specific peak, VELF rises more than SELF. Additionally, this figure demonstrates how the ITO content influences the peak positions and intensities of VELF and SELF for PV/CS/ITO nanocomposite films.

$$VELF = -\operatorname{lm}\left(\frac{1}{\varepsilon^*}\right) = \frac{\varepsilon^2}{\varepsilon_1^2+\varepsilon_2^2} \quad \text{..... Eq.12}$$

$$SELF = -\operatorname{lm}\left(\frac{1}{\varepsilon^*+1}\right) = \frac{\varepsilon_2}{(\varepsilon_1+1)^2+\varepsilon_2^2} \quad \text{..... Eq.13}$$

The optical conductivity (σ) of a material is a fundamental parameter used to characterize its optical response and is calculated using the following relation:

$$\sigma = \sigma_1 + j\sigma_2$$

$$\sigma_1 = \omega\epsilon_o\epsilon_2$$

$$\sigma_2 = \omega\epsilon_o\epsilon_1 \quad \text{..... Eq.14}$$

where, σ1 and σ2 denote the real and imaginary components of the optical conductivity, respectively, ω is the angular frequency of the incoming light, and εo is the permittivity of vacuum. The optical conductivity is intimately tied to the dielectric characteristics of the material, as it relies on both ε1 and ε2. Figure 12 (a&b) depicts the fluctuation in optical conductivity based on wavelength for PVA/ Chitosan/ITO nanocomposite films.

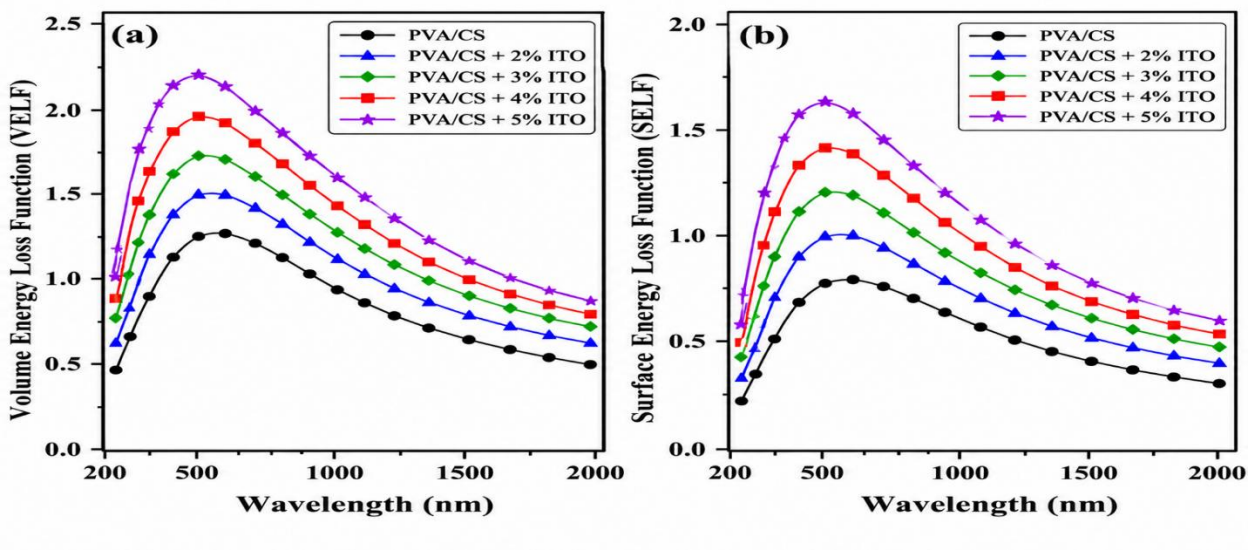


Fig. 12. Wavelength dependence of (a) VELF and (b) SELF for PVA/Chitosan/ITO nanocomposite films.

The optical conductivity is seen to rise with increased ITO content, especially in the wavelength range under 250 nm. The increase in σ values signifies a significantly excited electronic state or greater absorbance in the material, implying better charge carrier generation and transport characteristics.[13] Nonetheless, as the photon energy surpasses the absorption edge, the optical conductivity drops significantly, reflecting the material's optical band gap. This behavior aligns with the optical band gap values shown in Table 2, verifying the effect of ITO doping on the electronic structure of PVA/CS. The reduction in optical conductivity at elevated photon energies is linked to the diminished accessibility of electronic states for excitation and possible structural changes caused by the charge ordering effect. The incorporation of ITO nanoparticles into the PVA/CS matrix may lead to these structural changes, which are essential for defining the optical properties of the films. The improvement in optical conductivity with higher ITO levels underscores the promise of these nanocomposites for optoelectronic uses, including solar cells, photodetectors, and light-emitting devices, where effective charge carrier generation and transport are crucial. Investigating optical

conductivity offers essential understanding of the electronic and optical characteristics of PVA/ Chitosan/ITO nanocomposites, showcasing their adjustable properties and prospects for innovative technological uses.

Nonlinearity in PVA/ Chitosan/ITO nanocomposites films

Nonlinear optics (NLO) explores phenomena arising from the interaction of materials with high-intensity light, playing a critical role in photonics applications such as optical information processing, data storage, and sensor technologies. Organic materials, particularly those with π-conjugation, often exhibit strong NLO responses due to their electronic structure. In PVA/ Chitosan/ITO nanocomposite films, the NLO properties can be analyzed through the linear and nonlinear optical susceptibilities. The linear optical susceptibility ($\chi^{(1)}$) is determined using the next empirical relation based on the linear refractive index (n): [63–68]

$$\chi^{(1)} = \frac{n^2-1}{4\pi} \quad \text{..... Eq.15}$$

The third-order nonlinear susceptibility ($\chi^{(3)}$), which governs effects such as third-harmonic generation (THG), can be determined using a generalized form of Miller's rule:

$$\chi^{(3)} = A\left(\chi^{(1)}\right)^4 \quad \text{..... Eq.16}$$

where, A = 1.7×10^{-10} is a material-independent constant. The nonlinear refractive index (n_2) is related to $\chi^{(3)}$ and the static refractive index (n_0) by the following equation:

$$n_2 = \frac{12\pi\chi^{(3)}}{n_0} \quad \text{..... Eq.17}$$

Figure 13 (a&b) shows the changes in $\chi^{(3)}$ and n_2 with wavelength for PVA/ Chitosan/ITO nanocomposite films.

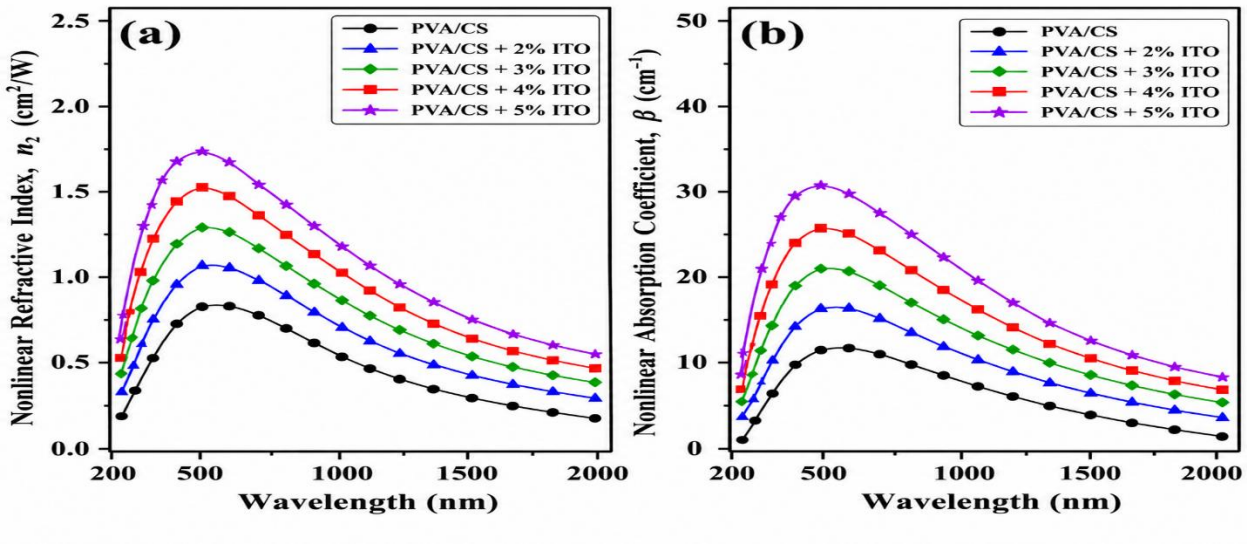


Fig. 13. Wavelength dependence of (a) the nonlinear refractive index (n_2) and (b) the nonlinear absorption coefficient (β) for PVA/Chitosan/ITO nanocomposite films

Both χ (3) and n2 show a downward trend as the wavelength increases when χ (3) and n2 are at zero-frequency (hυ = 0), nonetheless, the amount of ITO rises in the improvement on PVA/CS/ITO @MWCNT ($\chi^{(3)} = 20.37 \times 10^{-15}$ esu, $n_2 = 38.42 \times 10^{-14}$ esu at 0.01 MWCNT). The improvement in nonlinear optical characteristics is due to the heightened polarization of the polymer matrix with elevated ITO levels, enabling more effective absorption of electromagnetic waves and enhanced NLO responses. The decrease in the optical band gap with higher ITO content additionally enhances nonlinearity by promoting electronic transitions and generating charge carriers. The enhanced NLO characteristics of PVA/ Chitosan/ITO nanocomposites position them as promising options for nonlinear optoelectronic devices, including optical limiters, modulators, and switches. The addition of ITO nanoparticles into the PVA matrix brings Sn^{2+} free ions with significant polarizability and attached oxygen atoms, which account for the enhanced nonlinear optical parameters observed. The results indicate that raising the ITO concentration in the polymer matrix is a viable approach for modifying the NLO characteristics of the material, rendering it appropriate for cutting-edge photonic and optoelectronic uses.

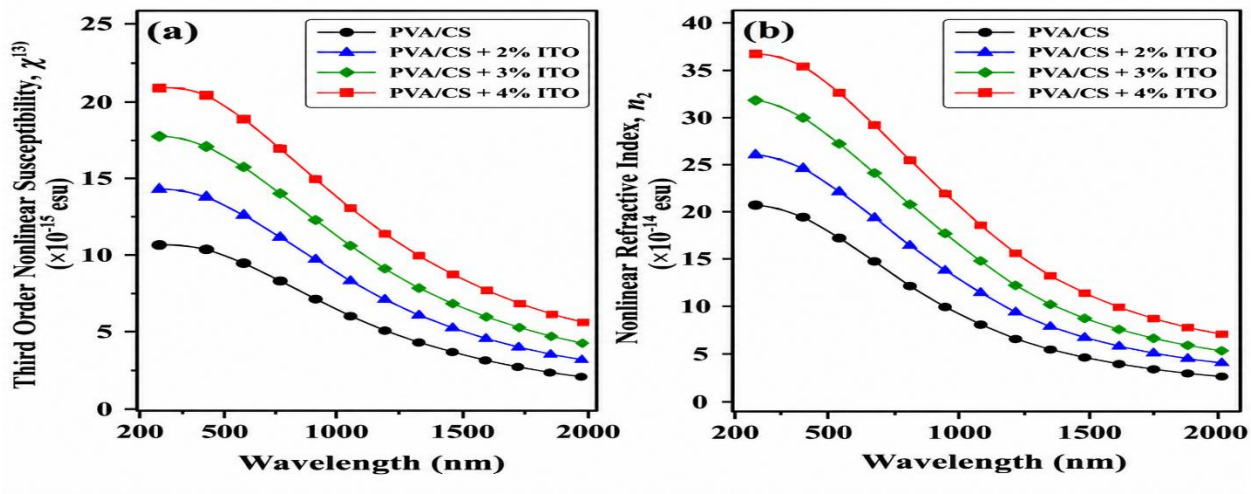


Fig. 14. The variation of (a) The third order non-linear susceptibility- $\chi^{(3)}$ and (b) The nonlinear refractive- n_2 vs. the wavelength for PVA/ Chitosan/ITO films.

The adjustable nonlinear optical characteristics of PVA/ Chitosan/ITO nanocomposite films, influenced by ITO concentration, underscore their promise for application in future generations' optical technologies. The interplay between structural modifications, electronic transitions, and polarizability underscores the importance of these materials in the field of nonlinear optics.

Conclusions

In this work, we systematically studied structural, optical, and photoluminescence properties of PVA/ Chitosan/ITO nanocomposite films, synthesized via a solution-casting technique. XRD confirmed that ITO incorporation reduced PVA's amorphous phase, increasing crystallite size by 28% (25.74 → 32.88 nm) while lowering dislocation density ($1.51 \times 10^{15} \rightarrow 0.92 \times 10^{15}$ m^{-2}). Homogeneous NP dispersion (< 3 wt %) transitions to aggregation at 5 wt% (SEM), establishing a critical loading threshold. FTIR spectroscopy confirmed the successful integration of ITO nanoparticles into the PVA/CS matrix, with distinct vibrational peaks corresponding to Sn-O bonds observed at 598 cm^{-1}. In addition, Specific E_g and $A_{1}g$ modes of ITO at 109 and 208 cm^{-1} were confirmed by Raman spectra. The band gap narrows from 4.59 eV (pristine PVA) to 4.18 eV (5 wt% ITO), enhancing semi conductivity. PL spectra revealed concentration-dependent quenching via PVA/ Chitosan/ITO cross-linking, with new defect-mediated emissions at 469/542 nm. Furthermore, the optical dielectric properties showed a rise with the higher ITO content, indicating enhanced polarizability and densification of the nanocomposite films. The nonlinear optical properties, such as $\chi^{(3)}$

and n_2, also exhibited a significant enhancement with increasing ITO concentration, making these materials promising candidates for use in flexible optoelectronic and nonlinear optical devices.

References

[1] Kotnik, T.; Kovačič, S. Eur. J. Org. Chem. 2025, 28, e202400874. https://doi.org/10.1002/ejoc.202400874.

[2] Nilsson, F.; Elf, P.; Capezza, A.; Wei, X.; Tsegaye, B.; et al. Sci. Total Environ. 2025, 958, 177926. https://doi.org/10.1016/j.scitotenv.2024.177926.

[3] DeMerlis, C. C.; Schoneker, D. R. Food Chem. Toxicol. 2003, 41, 319–326. https://doi.org/10.1016/S0278-6915(02)00258-2.

[4] Alghamdi, H. M.; Rajeh, A. Ceram. Int. 2025, 51, 18045–18055. https://doi.org/10.1016/j.ceramint.2025.01.581.

[5] Ramakoti, I. S.; Panda, A. K.; Gouda, N. J. Polym. Eng. 2023, 43, 651–679. https://doi.org/10.1515/polyeng-2023-0103.

[6] Abuelwafa, A. A.; Abd El-Sadek, M. S.; Elnobi, S.; Soga, T. Ceram. Int. 2021, 47, 13510–13518. https://doi.org/10.1016/j.ceramint.2021.01.209.

[7] Karthikeyan, B. Appl. Phys. A 2019, 125, 847. https://doi.org/10.1007/s00339-019-3136-1.

[8] Khedhri, M. H.; Lajnef, M.; Salhi, S.; Abdelmoula, N.; Khemakhem, H.; et al. Appl. Phys. A 2022, 128, 316. https://doi.org/10.1007/s00339-022-05432-0.

[9] Abdelhamid, S. M.; Dongol, M.; Elhady, A. F.; Abuelwafa, A. A. Discov. Appl. Sci. 2024, 6, 45. https://doi.org/10.1007/s42452-024-05638-2.

[10] Wemple, S. H.; DiDomenico, M. Phys. Rev. B 1971, 3, 1338–1351. https://doi.org/10.1103/PhysRevB.3.1338.

[11] Alharthi, S. S.; Badawi, A. Polymers 2023, 15, 2391. https://doi.org/10.3390/polym15102391.

[12] Soliman, T. S.; Vshivkov, S. A. J. Non-Cryst. Solids 2019, 519, 119452. https://doi.org/10.1016/j.jnoncrysol.2019.05.028.

[13] Heiba, Z. K.; El-Naggar, A. M.; Kamal, A. M.; Mohamed, M. B. Opt. Quantum Electron. 2024, 56, 235. https://doi.org/10.1007/s11082-023-05950-y.

[14] Kanchana, S. K.; Vanitha, N.; Basavaraj, R. B.; Madivalappa, S. Solid State Commun. 2023, 370, 115221. https://doi.org/10.1016/j.ssc.2023.115221.

[15] Rashad, M.; Abd-Elnaiem, A. M.; Hanafy, T. A.; Shaalan, N. M.; Shamekh, A. M. A. Opt. Mater. 2023, 141, 113990. https://doi.org/10.1016/j.optmat.2023.113990.

[16] Puttaswamy, M. P.; Subramani, N. K.; Shivanna, S.; Siddamallappa, N. G.; Madhukar, B. S.; et al. Mater. Sci. Semicond. Process. 2025, 193, 109484. https://doi.org/10.1016/j.mssp.2025.109484.

[17] Elhosiny, A.; Algarni, H.; Khairy, H. Opt. Mater. 2020, 108, 110212. https://doi.org/10.1016/j.optmat.2020.110212.

[18] Rashad, M. Opt. Mater. 2020, 105, 109857. https://doi.org/10.1016/j.optmat.2020.109857.

[19] Osemba, M. O.; Karenga, S.; Keru, G. Int. J. Pure Appl. Chem. 2026, 4(1), 1–13. https://doi.org/10.37284/ijpac.4.1.4336.

[20] Osemba, M. O.; Muriuki-Hutchins, M.; Karenga, S.; Keru, G. Int. J. Adv. Res. 2024, 7(1), 244–250. https://doi.org/10.37284/ijar.7.1.2193.

[21] Mutuku, D.; Osemba, M. O.; Thoruwa, T.; Keheze, F. Effect of chitosan coating on the efficiency and degradation of solar panels. 2025. https://doi.org/10.5281/zenodo.17663343.

[22] Osemba, M. O. Microwave-assisted starch stabilization and chitosan green synthesis of zinc oxide nanoparticles for photocatalytic applications. Research Square preprint, 2026. https://doi.org/10.21203/rs.3.rs-9131972/v1.

[23] Osemba, M. O.; Chávez Huerta, A.; Keru, G. Graphene quantum dot–MXene nano-optoelectronic interface for ultrasensitive photoelectrochemical detection of emerging water contaminants. ChemRxiv preprint, 2026. https://doi.org/10.26434/chemrxiv.15007088/v1.

[24] Osemba, M. O.; Chávez Huerta, A.; Maghanga, J. K. Structural, optical, dielectric and nonlinear properties of PVA/Na-alginate/ITO nanocomposite films. Research Square preprint, 2026. https://doi.org/10.21203/rs.3.rs-9366243/v1.

[25] Osemba, M. O.; Chávez Huerta, A.; Karenga, S.; Keru, G. Surface functionalization and interfacial chemistry in PVDF/$BaTiO_3$/graphene nanocomposites for enhanced dielectric performance. Research Square preprint, 2026. https://doi.org/10.21203/rs.3.rs-9370521/v1.

[26] Rinaudo, M. Chitin and chitosan: Properties and applications. Prog. Polym. Sci. 2006, 31, 603–632. https://doi.org/10.1016/j.progpolymsci.2006.06.001.

[27] Dash, M.; Chiellini, F.; Ottenbrite, R. M.; Chiellini, E. Chitosan—A versatile semi-synthetic polymer in biomedical applications. Prog. Polym. Sci. 2011, 36, 981–1014. https://doi.org/10.1016/j.progpolymsci.2011.02.001.

[28] Pillai, C. K. S.; Paul, W.; Sharma, C. P. Chitin and chitosan polymers: Chemistry, solubility and fiber formation. Prog. Polym. Sci. 2009, 34, 641–678. https://doi.org/10.1016/j.progpolymsci.2009.04.001.

[29] Berger, J.; Reist, M.; Mayer, J. M.; Felt, O.; Peppas, N. A.; Gurny, R. Structure and interactions in covalently and ionically crosslinked chitosan hydrogels for biomedical applications. Eur. J. Pharm. Biopharm. 2004, 57, 19–34. https://doi.org/10.1016/j.ejpb.2003.10.003.

[30] Khor, E.; Lim, L. Y. Implantable applications of chitin and chitosan. Biomaterials 2003, 24, 2339–2349. https://doi.org/10.1016/S0142-9612(03)00017-0.

[31] Jayakumar, R.; Prabaharan, M.; Nair, S. V.; Tamura, H. Novel chitin and chitosan nanofibers in biomedical applications. Biotechnol. Adv. 2010, 28, 142–150. https://doi.org/10.1016/j.biotechadv.2009.11.001.

[32] Sionkowska, A. Current research on the blends of natural and synthetic polymers as new biomaterials: Review. Prog. Polym. Sci. 2011, 36, 1254–1276. https://doi.org/10.1016/j.progpolymsci.2011.05.003.

[33] Alexandre, M.; Dubois, P. Polymer-layered silicate nanocomposites: Preparation, properties and uses of a new class of materials. Mater. Sci. Eng. R 2000, 28, 1–63. https://doi.org/10.1016/S0927-796X(00)00012-7.

[34] Pavlidou, S.; Papaspyrides, C. D. A review on polymer–layered silicate nanocomposites. Prog. Polym. Sci. 2008, 33, 1119–1198. https://doi.org/10.1016/j.progpolymsci.2008.07.008.

[35] Kango, S.; Kalia, S.; Celli, A.; Njuguna, J.; Habibi, Y.; Kumar, R. Surface modification of inorganic nanoparticles for development of organic–inorganic nanocomposites—A review. Prog. Polym. Sci. 2013, 38, 1232–1261. https://doi.org/10.1016/j.progpolymsci.2013.02.003.

[36] Jordan, J.; Jacob, K. I.; Tannenbaum, R.; Sharaf, M. A.; Jasiuk, I. Experimental trends in polymer nanocomposites—A review. Mater. Sci. Eng. A 2005, 393, 1–11. https://doi.org/10.1016/j.msea.2004.09.044.

[37] Paul, D. R.; Robeson, L. M. Polymer nanotechnology: Nanocomposites. Polymer 2008, 49, 3187–3204. https://doi.org/10.1016/j.polymer.2008.04.017.

[38] Ruiz-Hitzky, E.; Darder, M.; Aranda, P. Functional biopolymer nanocomposites based on layered solids. J. Mater. Chem. 2010, 20, 9306–9321. https://doi.org/10.1039/C0JM01324E.

[39] Darder, M.; Colilla, M.; Ruiz-Hitzky, E. Biopolymer–clay nanocomposites based on chitosan intercalated in montmorillonite. Chem. Mater. 2003, 15, 3774–3780. https://doi.org/10.1021/cm021217b.

[40] Granqvist, C. G. Transparent conductors as solar energy materials: A panoramic review. Sol. Energy Mater. Sol. Cells 2007, 91, 1529–1598. https://doi.org/10.1016/j.solmat.2007.04.031.

[41] Minami, T. Transparent conducting oxide semiconductors for transparent electrodes. Semicond. Sci. Technol. 2005, 20, S35–S44. https://doi.org/10.1088/0268-1242/20/4/004.

[42] Ellmer, K. Past achievements and future challenges in the development of optically transparent electrodes. Nat. Photonics 2012, 6, 809–817. https://doi.org/10.1038/nphoton.2012.282.

[43] Fortunato, E.; Ginley, D.; Hosono, H.; Paine, D. C. Transparent conducting oxides for photovoltaics. MRS Bull. 2007, 32, 242–247. https://doi.org/10.1557/mrs2007.29.

[44] Hecht, D. S.; Hu, L.; Irvin, G. Emerging transparent electrodes based on thin films of carbon nanotubes, graphene, and metallic nanostructures. Adv. Mater. 2011, 23, 1482–1513. https://doi.org/10.1002/adma.201003188.

[45] Hamberg, I.; Granqvist, C. G. Evaporated Sn-doped In_2O_3 films: Basic optical properties and applications to energy-efficient windows. J. Appl. Phys. 1986, 60, R123–R160. https://doi.org/10.1063/1.337080.

[46] Ohta, H.; Hosono, H. Transparent oxide optoelectronics. Mater. Today 2004, 7, 42–51. https://doi.org/10.1016/S1369-7021(04)00208-0.

[47] Ginley, D. S.; Bright, C. Transparent conducting oxides. MRS Bull. 2000, 25, 15–18. https://doi.org/10.1557/mrs2000.226.

[48] Tauc, J.; Grigorovici, R.; Vancu, A. Optical properties and electronic structure of amorphous germanium. Phys. Status Solidi 1966, 15, 627–637. https://doi.org/10.1002/pssb.19660150224.

[49] Davis, E. A.; Mott, N. F. Conduction in non-crystalline systems V. Conductivity, optical absorption and photoconductivity in amorphous semiconductors. Philos. Mag. 1970, 22, 903–922. https://doi.org/10.1080/14786437008221061.

[50] Cody, G. D.; Tiedje, T.; Abeles, B.; Moustakas, T. D.; Brooks, B. Optical absorption edge in a-Si:H. Phys. Rev. Lett. 1981, 47, 1480–1483. https://doi.org/10.1103/PhysRevLett.47.1480.

[51] Swanepoel, R. Determination of the thickness and optical constants of amorphous silicon. J. Phys. E: Sci. Instrum. 1983, 16, 1214–1222. https://doi.org/10.1088/0022-3735/16/12/023.

[52] Manifacier, J. C.; Gasiot, J.; Fillard, J. P. A simple method for the determination of the optical constants n, k and the thickness of a weakly absorbing thin film. J. Phys. E: Sci. Instrum. 1976, 9, 1002–1004. https://doi.org/10.1088/0022-3735/9/11/1002.

[53] Moss, T. S. A relationship between the refractive index and the infra-red threshold of sensitivity for photoconductors. Proc. Phys. Soc. B 1950, 63, 167–176. https://doi.org/10.1088/0370-1301/63/3/306.

[54] Ravindra, N. M.; Srivastava, V. K.; Auluck, S. On the Penn gap in semiconductors. Infrared Phys. 1979, 19, 603–604. https://doi.org/10.1016/0020-0891(79)90062-7.

[55] Hervé, P.; Vandamme, L. B. X. General relation between the refractive index and the energy gap in semiconductors. Infrared Phys. Technol. 1994, 35, 609–615. https://doi.org/10.1016/1350-4495(94)90026-4.

[56] Miller, R. C. Optical second harmonic generation in piezoelectric crystals. Appl. Phys. Lett. 1964, 5, 17–19. https://doi.org/10.1063/1.1753922.

[57] Sheik-Bahae, M.; Said, A. A.; Van Stryland, E. W. High-sensitivity, single-beam n_2 measurements. Opt. Lett. 1989, 14, 955–957. https://doi.org/10.1364/OL.14.000955.

[58] Sheik-Bahae, M.; Said, A. A.; Wei, T. H.; Hagan, D. J.; Van Stryland, E. W. Sensitive measurement of optical nonlinearities using a single beam. IEEE J. Quantum Electron. 1990, 26, 760–769. https://doi.org/10.1109/3.53394.

[59] Sheik-Bahae, M.; Hagan, D. J.; Van Stryland, E. W. Dispersion and band-gap scaling of the electronic Kerr effect in solids associated with two-photon absorption. Phys. Rev. Lett. 1991, 65, 96–99. https://doi.org/10.1103/PhysRevLett.65.96.

[60] Hache, F.; Ricard, D.; Flytzanis, C. Optical nonlinearities of small metal particles: Surface-mediated resonance and quantum size effects. J. Opt. Soc. Am. B 1988, 5, 1131–1142. https://doi.org/10.1364/JOSAB.5.001131.

[61] Gorrasi, G.; Sorrentino, A. Photo-oxidative stabilization of carbon nanotubes and polymer nanocomposites. Polymers 2015, 7, 305–320. https://doi.org/10.3390/polym7030305.

[62] Mittal, V. Polymer nanocomposites: Advances in filler surface modification and characterization. Materials 2009, 2, 992–1057. https://doi.org/10.3390/ma2030992.

[63] Mittal, V. Polymer layered silicate nanocomposites: A review. Materials 2014, 7, 7198–7265. https://doi.org/10.3390/ma7097198.

[64] Kotal, M.; Bhowmick, A. K. Polymer nanocomposites from modified clays: Recent advances and challenges. Prog. Polym. Sci. 2015, 51, 127–187. https://doi.org/10.1016/j.progpolymsci.2015.04.002.

[65] Thomas, S.; Thomas, M. G.; Zachariah, A. K.; Mishra, R. K. Polymer nanocomposites: Preparation and properties. Prog. Polym. Sci. 2010, 35, 1003–1050. https://doi.org/10.1016/j.progpolymsci.2010.03.003.

[66] Sahoo, S.; Kundu, P. P.; Kumar, R. Polymer nanocomposites: Processing, characterization and applications. Prog. Polym. Sci. 2010, 35, 1029–1057. https://doi.org/10.1016/j.progpolymsci.2010.03.002.

[67] Kausar, A. Polymer/clay nanocomposites: Design and applications. Polym. Plast. Technol. Eng. 2018, 57, 1–20. https://doi.org/10.1080/03602559.2017.1329438.

[68] Decher, G. Fuzzy nanoassemblies: Toward layered polymeric multicomposites. Science 1997, 277, 1232–1237. https://doi.org/10.1126/science.277.5330.1232.

[69] Bergman, L.; McHale, J. L. Handbook of Luminescent Semiconductor Materials. J. Lumin. 2010, 130, 1–10. https://doi.org/10.1016/j.jlumin.2009.07.015.

[70] Kumar, M. N. V. R. A review of chitin and chitosan applications. React. Funct. Polym. 2000, 46, 1–27. https://doi.org/10.1016/S1381-5148(00)00038-9.